Supplementary Information – Phonon-like hydrogen-bond modes in protic ionic liquids

Judith Reichenbach, Stuart A. Ruddell, Mario González-Jiménez, Julio Lemes, David A. Turton, David J. France, and Klaas Wynne*

School of Chemistry, WestCHEM, University of Glasgow, UK,

MATERIALS

Sample preparation. Tetrabutylammonium chloride (≥ 99.0%, Sigma Aldrich), tetrabutylammonium bromide (≥ 98.0%, Sigma Aldrich), tributylmethylammonium chloride (≥ 98.0%, Sigma Aldrich) and tributylmethylammonium bromide (≥ 98.0%, Sigma Aldrich) were used without further purification. Tributylammonium chloride (≥ 95%) and tributylammonium bromide (≥ 95%) were synthesized and their purity confirmed by ^{1}H-NMR (see SI). All ILs were dried as powders for at least 16 hours at approximately 70 °C under vacuum before use. Any further handling was done in a glove box under dry nitrogen (≥ 99.998%, BOC).

Synthesis of Tributylammonium bromide

Following the procedure of Hojo *et al.*,[1a] 1 equivalent of a 10 vol-% solution of aqueous hydrogen bromide (48% w/w, Lancaster) in methanol (≥ 99.7%, Sigma Aldrich) was added under stirring to 1 equivalent of tributylamine (≥ 99.5%, Sigma Aldrich) at room temperature and kept stirring for 30 minutes. The excess solvent was evaporated to dryness at below 50 °C in a rotary evaporator with a saturated aqueous potassium carbonate trap, which gave a yellow salt. This was recrystallized from hot methanol, filtered and then washed with cold diethyl ether (≥ 99.8%, Sigma Aldrich), giving a pale yellow solid, with an 88% yield.

^{1}H-NMR (400 MHz, DMSO d_6) δ 8.99 (1 H, br s), 3.03 (6 H, dt, J = 12.1 Hz, 4.8 Hz), 1.63 – 1.55 (6 H, m), 1.32 (6 H, tq, J = 7.4 Hz, 7.4 Hz), 0.92 (9 H, t, J = 7.3 Hz). HRMS (ESI) exact mass calculated for $C_{12}H_{28}N$ [M]$^+$ m/z 186.2216, found m/z 186.2213. Microanalysis calculated for $C_{12}H_{28}NBr$: C, 54.13; H, 10.60; N, 5.26. Found: C, 54.16; H, 10.65; N, 5.32.

Synthesis of Tributylammonium chloride

Following the procedure of Fumino *et al.*,[1b] 1 M hydrogen chloride in diethyl ether (Sigma Aldrich) was added to tributylamine (≥ 99.5%, Sigma Aldrich) while cooling to 0 °C. After maintaining for 30 min at 0 °C, volatile components were removed by rotary evaporator, affording the ammonium chloride salt in quantitative yield.

^{1}H-NMR (500 MHz, DMSO d_6) δ 10.70 (1 H, br s), 2.96 (6 H, dt, J = 12.4 Hz, 4.8 Hz), 1.67 – 1.60 (6 H, m), 1.30 (6 H, tq, J = 7.5 Hz, 7.5 Hz), 0.90 (9 H, t, J = 7.4 Hz). HRMS (ESI) exact mass calculated for C12H28N [M]+ m/z 186.2216, found m/z 186.2213. Microanalysis calculated for C12H28NCl: C, 64.98; H, 12.72; N, 6.31. Found: C, 64.49; H, 12.67; N, 6.44.

EXPERIMENTAL DETAILS

Far-IR experimental details. The far-IR data were taken using a dry-air purged Bruker Vertex 70 spectrometer equipped with a mercury arc lamp, a DLaTGS detector, and a silicon solid-state beamsplitter. For the liquid spectra, a drop of the respective liquid was sandwiched between two 2-mm thickness TPX (poly(4-methyl-1-pentene)) windows in a preheated temperature-controlled liquid cell (Harrick Scientific, precision ± 1.5 °C) using a 10 μm or 56 μm PTFE ring spacer. 128 scans were taken between 30 and 600 cm^{-1} with 5-cm^{-1} resolution. For the pellet spectra, 1 volume equivalent of ionic liquid powder was mixed with polyethylene powder (40-48 μm diameter, Sigma Aldrich) in an agate mortar and pressed into 7-mm pellets using a hand press (Pike Technologies). 64 scans were taken at room temperature between 30 and 400 cm^{-1} with 2-cm^{-1} resolution.

OKE experimental details. The powdered ionic liquids were transferred into modified rectangular quartz cuvettes (Starna, thickness 1 or 2 mm), which were equipped with a valve and a connector for tubing. The solid was melted inside the cuvette. During the melting process, reduced pressure and dry nitrogen were applied as necessary to avoid gas bubbles becoming trapped in the liquid.

The OKE data were taken in a purpose-built time-domain pump-probe setup[2-3] using a Coherent Micra laser oscillator with a repetition rate of 82 MHz. The laser pulses had an energy of ~10 nJ (0.8 W average power) and were centered at 800 nm with a pulse width of 21 to 25 fs. Measurements were taken with delay times of up to 1 ns resulting in spectral coverage down to 1 GHz (< 0.033 cm^{-1}) in the frequency domain after numerical Fourier transformation. Samples were held in quartz cuvettes inside a temperature-controlled aluminum block with a precision of ± 0.1 °C.
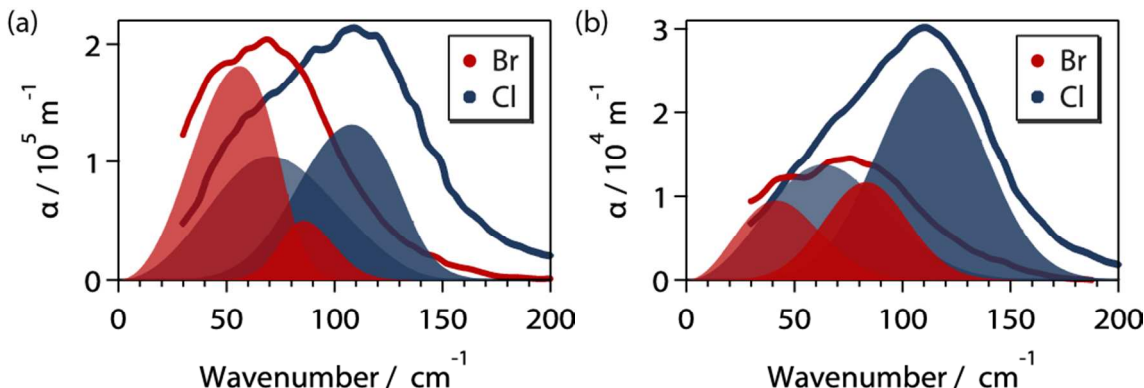
ADDITIONAL DATA

Figure SI1. Effect of changing the anion on the terahertz frequency-domain far-IR spectra. (a) Comparison of the far-IR spectra of liquid tetrabutylammonium chloride and bromide. (b) Comparison of the far-IR spectra of liquid tributylme-thylammonium chloride and bromide. The absorption coefficient of tributylmethylammonium bromide was underestimated in the measurement due to irremovable bubbles in the sample.

DATA ANALYSIS

A simple relation between OKE and far-IR spectroscopy

As described previously,[4] both OKE and far-IR spectra are proportional to a frequency-domain response function that has the same form for both techniques but different amplitudes for the individual components that make up the total response, *i.e.*,

$$R^{OKE/IR}(\omega) = \sum_i A_i^{OKE/IR} R_i(\omega) . \tag{SI1}$$

In this work, the individual component responses are represented by fit functions as described below. In systems with very high symmetry (in particular, for intramolecular vibrational modes in molecules with high symmetry), the amplitudes will be quite different. However, for low frequency intermolecular modes these amplitudes should be of comparable magnitude. Using this response function, the dielectric function $\varepsilon(\omega)$ can be written as

$$\varepsilon(\omega) = \varepsilon_{\text{inf}} + R^{IR}(\omega) , \tag{SI2}$$

where ε_{inf} is the infinite frequency relative dielectric constant, while the OKE spectrum can be written as

$$S_{OKE}(\omega) = \text{Im} R^{OKE}(\omega) . \tag{SI3}$$

In this work, we measure IR absorbance rather than the dielectric function. The absorbance (A) measured by our FTIR instrument is transformed into the absorption coefficient $\alpha(\omega)$ using Lambert's law

$$10^{-A} = e^{-\alpha(\omega)d} , \tag{SI4}$$

in which d is the sample thickness. The absorption coefficient $\alpha(\omega)$ and the refractive index $n(\omega)$ are related to the complex refractive index $\tilde{n}(\omega)$, which is given by the square root of the dielectric function, that is,

$$\tilde{n}(\omega) = \sqrt{\varepsilon(\omega)} = n(\omega) + i\frac{c\alpha(\omega)}{2\omega},\tag{SI5}$$

with c the speed of light. This leads to

$$\alpha(\omega) = \frac{2\omega}{c}Im[\tilde{n}(\omega)].\tag{SI6}$$

Some of the samples studied here have very strong absorption bands in the far-IR giving rise to large refractive index changes well above the high-frequency refractive indices of ionic liquids ($n_D \sim 1.4$-1.5) and the window material, TPX ($n_{FIR} = 1.46$)[5-8] resulting in significant interfacial reflections. By incorporating Fresnel reflections using transmission coefficients defined by

$$T_{ij} = 2n_i/(n_i + n_j) \,,\tag{SI7}$$

where i and j are equal to window (w) or sample (s), one can relate the experimentally measured absorption coefficient α_{exp} with the actual absorption coefficient α by

$$I/I_0 = e^{-\alpha_{exp}(\omega)d} = e^{-\alpha(\omega)d}T_{ws}^2 T_{sw}^2,\tag{SI8}$$

where d is the sample thickness and multiple reflections have been ignored.

It is often useful to show the individual components of a fit to OKE or far-IR data in a figure. This presents no problem in the case of OKE but is more involved in the case of far-IR. The visualization of the individual components in the OKE spectrum is trivial because the fit is a simple superposition. In the far-IR spectrum, on the other hand, the influence of the real part of the dielectric function on each mode needs to be taken into account. Thus, Eq. (SI6) cannot be used to plot individual fit functions in the far-IR. However, Eq. (SI6) can be written as

$$\alpha(\omega) \cong \frac{\omega\,Im[\varepsilon(\omega)]}{c\,Re[\sqrt{\varepsilon(\omega)}]}\tag{SI9}$$

in the limit $Im[\varepsilon(\omega)] \to 0$, which allows us to plot the absorption of an individual component using[4]

$$\alpha_i(\omega) \cong \frac{\omega\,Im[f_i(\omega)]}{c\,Re\left[\sqrt{\sum_k f_k(\omega)}\right]}\,.\tag{SI10}$$

Fit functions

The measured terahertz spectra were fitted with a set of empirical functions often used to describe dynamics in the terahertz range.[9] These are the Havriliak-Negami, the Brownian oscillator, and the anti-symmetrized Gaussian functions, which are described in further detail below. In order to fit the far-IR absorption data, the complex dielectric function is needed (Eq. (SI6)) in contrast to the OKE data (Eq. (SI3)), which only uses the imaginary part. Therefore, complex fit models are required that represent the real and imaginary part of the dielectric function.

Anti-symmetrized Gaussian

In OKE spectra, anti-symmetrized Gaussian functions[9] are often used to fit intermolecular modes such as librations that are inhomogeneously broadened due to a distribution of environments. The complex anti-symmetrized Gaussian can be found using the Kramers-Kronig relations and is given by

$$G(\omega) = A_G e^{\frac{-(\omega-\omega_0)^2}{\gamma^2}}\left(i - erfi\left[\frac{\omega-\omega_0}{\gamma}\right]\right) - A_G e^{\frac{-(\omega+\omega_0)^2}{\gamma^2}}\left(i - erfi\left[\frac{\omega+\omega_0}{\gamma}\right]\right),\tag{SI11}$$

where ω is the angular frequency, A_G is the amplitude, ω_0 is the undamped-oscillator angular frequency, γ is a damping parameter, and $erfi(z)$ is the imaginary error function defined by

$$erfi(z) \equiv erf(iz)/i\tag{SI12}$$
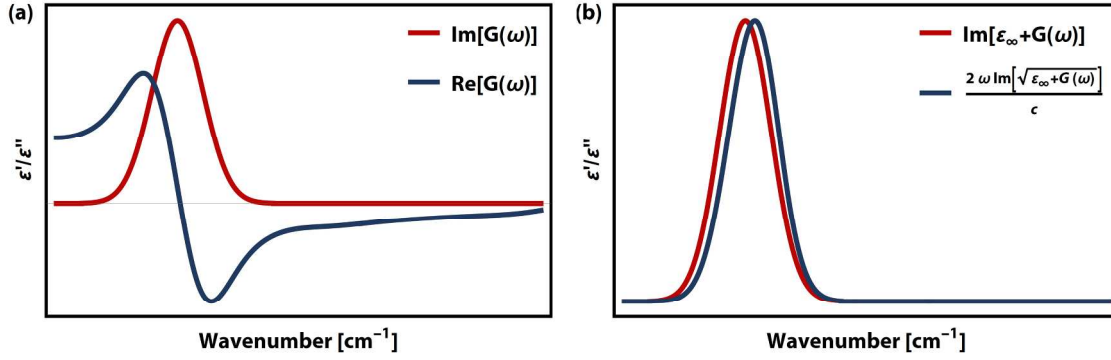
with the error function $erf(x)$.

Figure SI2. Plots of the anti-symmetrized Gaussian function. (a) Shown are the real (blue) and imaginary (red) part of an anti-symmetrized Gaussian function with central oscillator frequency set to 100 cm^{-1}. (b) Scaled comparison between the shape of a single anti-symmetrized Gaussian function after being transformed for fitting to OKE (red) and far-IR data (blue).

Brownian oscillator

The Brownian oscillator function[9] is often used to model homogeneously-broadened intramolecular modes. In the frequency domain, the Brownian oscillator is defined by

$$B(\omega) = \frac{A_B \omega_0^{\,2}}{\omega_0^{\,2} - \omega(\omega + 2i\gamma)} \; , \tag{SI13}$$
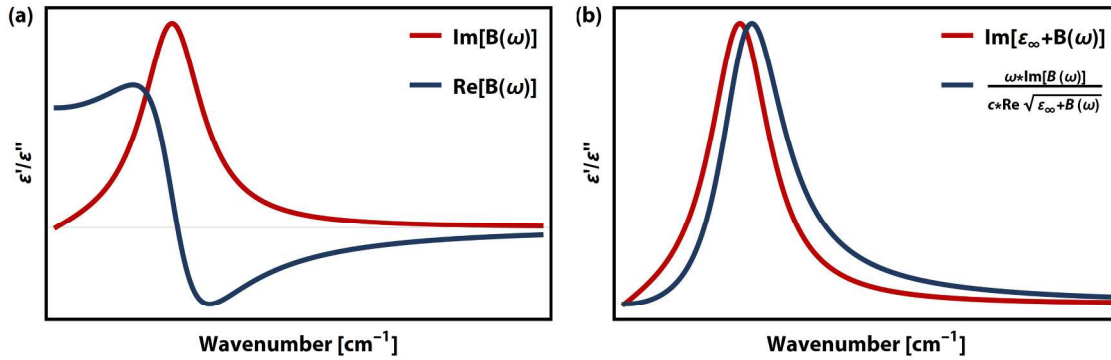
where A_B is the amplitude.

Figure SI3. Plots of the Brownian oscillator function. (a) Shown are the real (blue) and imaginary (red) part of a Brownian oscillator with oscillator frequency set to 100 cm^{-1}. (b) Scaled comparison between the shape of a single Brownian oscillator after being transformed for fitting to OKE (red) and far-IR data (blue).

Havriliak-Negami: diffusive relaxation

The Havriliak-Negami function is commonly used to model diffusive relaxation[9] and can be written in the frequency domain as

$$H_{\alpha,\beta}(\omega) = \frac{A_{HN}}{\left(1 + (-i\omega\tau)^\alpha\right)^\beta} \; , \tag{SI14}$$

where A_{HN} is the amplitude and τ is the orientational relaxation time. Here α and β are broadening and asymmetry parameters taking on values between zero and one. If both α and β are restrained to a value of 1, the Havriliak-Negami function turns into the **Debye function**, which corresponds with an exponential decay in the time domain. The Debye function is mostly used to model the slowest diffusive orientational relaxation band. All Havriliak-Negami functions were α and β do not both equal 1 can be interpreted as superpositions of Debye functions with a distribution of relaxation times. When $\alpha = 1$, the Havriliak-Negami function reduces to a **Cole-**

Davidson function, which is asymmetrically broadened, having a less steep slope on the high frequency side. When $\beta = 1$, the Havriliak-Negami function reduces to a **Cole-Cole function**, which is symmetrically broadened with respect to the Debye function and as such shows less steep slopes on both sides. Cole-Cole functions with a small value in α have been used previously[9] to model translational diffusive relaxations that resemble white noise in the time domain.

The Havriliak-Negami function falls off too slowly at high frequencies, which is unphysical and affects the overall fit.[9-10] This is caused by the discontinuous rise of its time domain equivalent at $t = 0$, which can be corrected by multiplying with a rise function to give a physical solution, *i.e.*,

$$F'(t) = F(t)\left(1 - e^{-\Gamma t}\right), \tag{SI15}$$

where $F(t)$ stands for the function that will be modified, t is time, and Γ is a rise parameter. An exponential form is chosen for the rise function because it yields a general Fourier transform without having to take into account the convolution with the Havriliak-Negami function. Fourier transforming this into the frequency domain yields

$$F'(\omega) = F(\omega) - F(\omega + i\Gamma), \tag{SI16}$$

which can be used on functions without an analytical Fourier transform in the time domain. The rise parameter cannot be measured. However, it is insensitive to small changes and can be estimated from values such as the free rotation time or the librational frequency.[10]

The Havriliak-Negami function as shown works well for fitting OKE spectra. Using our far-IR transformation (Eq. (SI6)), however, yields a behavior not consistent with the observed spectra. An unmodified Debye function will, at high frequency, go to a constant value due to the multiplication with the frequency in the transformation. The other variants of the Havriliak-Negami function will diverge at high frequency. The rise modification will suppress this behavior, however the exponential used is only strong enough to modify the Debye function satisfactorily. As such, only the Debye function was used in any further fits.
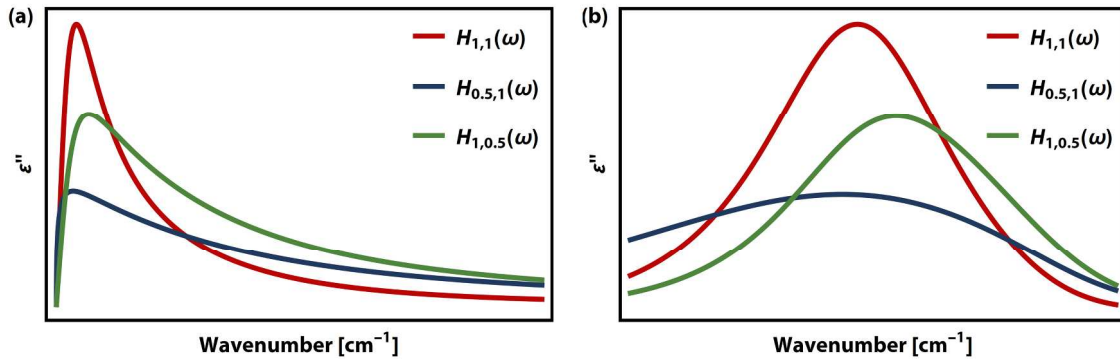
Figure SI4. Linear (a) and logarithmic (b) plots of rise-modified Havriliak-Negami functions with different α and β parameters. The differences between a Debye function ($H_{1,1}$), a Cole-Cole function ($H_{0.5,1}$) and a Cole-Davidson function ($H_{1,0.5}$) are most obvious in the logarithmic plot.

CURVE FITTING PROCEDURES

All the weighted nonlinear least-squares curve fits were carried out with a program written in Mathematica (Wolfram Mathematica 10 & 11). For each sample both the data sets from OKE and far-IR were loaded into the program. A function was then fitted to both data sets simultaneously using the in-built *NonlinearModelFit*. The weights depended on the frequency as well as the maximum intensity. They were given by

$$w_s(f) = \frac{1}{I_{s,\max}^2} \begin{cases} f & , f \leq 1\,\text{THz} \\ 1 & , 1\,\text{THz} < f > 10\,\text{THz} \\ \dfrac{10^3}{f^3} & , f \geq 10\,\text{THz} \end{cases}, \qquad \text{(SI17)}$$

with $I_{s,\max}$ denoting the maximum intensity of either the OKE or far-IR spectrum and f being given in THz. Note that far-IR data is only measured at frequencies >1 THz. The weighting takes into account that the far-IR data become increasingly noisy due absorption by the window material (TPX) at high frequencies. The origin of the high and low frequency weights in the OKE spectrum is less straightforward and is due to errors caused by the Fourier transform of the measured time domain data. At low frequencies, random errors occur if the measured time was not long enough to fully capture the slowest relaxation. The high frequency limit, on the other hand, is given by the pulse width and errors usually manifest themselves as changes in the slope of the spectrum.

While it can be seen from Eq. (SI3) that the real part of the dielectric function has no influence on the OKE spectra, Eq. (SI6) shows that it cannot be neglected in the far-IR spectra. The real part of the dielectric function is connected to the refractive index (see Eq. (SI5)). Due to the limited frequency range of the far-IR measurement it is not possible to fully fit the real part of the dielectric function. As such a constant, $\varepsilon_\infty = n_\infty^2$, has to be added to the superposition of fit functions, $\tilde{\varepsilon}(\omega) = \varepsilon_\infty + \sum_i \tilde{f}_i(\omega)$, to take into account the influence of the refractive index at higher frequencies. This was estimated as $n_\infty = 1.5$ since the refractive index at 589 nm of alkylammonium ILs varies between 1.4 and 1.5.[6-8] For the reflection corrections in the far-IR it was also necessary to use the refractive index of TPX, $n_{TPX} = 1.457$, which is approximately frequency independent in the far-infrared, varying between 1.4555 and 1.4570.[5]

Further approximations were made to the imaginary error function, $erfi(z)$, used in the anti-symmetrized Gaussian to increase the speed of the calculations compared to the imaginary error function built into Mathematica. For this the error function with complex arguments, $erf(z) = erf(x+iy)$, was defined using the method outlined by Salzer[11] in the case of $\text{Re}[z] = 0$, leading to

$$erf(0+iy) = \frac{iy}{\pi} + \frac{2i}{\pi} \sum_n \frac{\sinh[ny]}{n} e^{-\frac{n^2}{4}}. \qquad \text{(SI18)}$$

In the present case, it can be seen from the definition of the anti-symmetrized Gaussian, Eq. (SI11), that the argument given to the imaginary error function will always be purely real. Thus, we can use Eq. (SI18) in Eq. (SI12) to get

$$erfi(x+0i) = \frac{x}{\pi} + \frac{2}{\pi} \sum_n \frac{\sinh[nx]}{n} e^{-\frac{n^2}{4}} \qquad \text{(SI19)}$$

for the imaginary error function. In this, n ran from 1 to 20 to balance speed and precision.

Additional approximations were made in the anti-symmetrized Gaussian to avoid errors due to very small or large numbers and to speed up computations. The definition of the anti-symmetrized Gaussian, Eq. (SI11), can be split up into four terms in which the dominant factor is either an exponential or the product of an exponential and the imaginary error function. These terms can be written as

$$iAe^{\Omega_\pm^2} \qquad \text{(SI20)}$$

$$Ae^{\Omega_\pm^2} erfi(\Omega_\pm) \qquad \text{(SI21)}$$

with $\Omega_\pm = (\omega \pm \omega_0)/\gamma$. Each term was set to zero once the value of the exponential, for Eq. (SI20), or the product of the exponential and the imaginary error function, for Eq. (SI21), was less than 10^{-3}. For the terms following

Eq. (SI20), this was the case for $|\Omega| \geq 2.63$ and for the terms following Eq. (SI21) this was reached when $|\Omega| \geq 11.71$.

In the definition of all functions separate far-IR and OKE amplitudes, A_{IR} and A_{OKE}, were used instead of one amplitude. This allowed the use of the exact same functions (apart from amplitude) in both the OKE and far-IR fit simultaneously. If a band was clearly symmetry excluded in one spectrum, the corresponding amplitude was simply set to zero.

Fitting procedure

Due to the general scarceness of features in the alkylammonium IL spectra, a good starting estimate of the fit parameters was essential. To determine these, a number of steps were used. Firstly, two anti-symmetrized Gaussians were placed in the far-IR spectrum. In the protic ILs, these were placed on the two distinctive bands. In the aprotic ILs one anti-symmetrized Gaussian was each placed at the low and high frequency end of the main band, respectively, and the damping was initially based on the damping of the corresponding band in the protic IL spectrum. The oscillator frequencies were also compared to those found in the solid spectra and adjusted if necessary. Another anti-symmetrized Gaussian was then added to correct for the slope on the high-frequency side of the main band.

In the second step a Debye function was placed at the low frequency end of the OKE spectrum and all OKE amplitudes were varied to fit the main band. In the last step Brownian oscillators were added to model the vibrational bands at the high frequency end of the spectrum.

After this, parameters were varied in small batches by the fitting algorithm and additional functions were added to improve the fit if necessary. This was found to result in a stable and unique fits to the experimental data in all liquids studied. The most difficult to fit were the data taken in the tetrabutylammonium salts (due to the overlap of the A and C band and the significant effect of refractive-index changes), however, the validity of these fits is confirmed by the solid-state far-IR spectra.

FIT PARAMETERS

Table SI1. *Fit parameters for the measured ionic liquids. For the Debye functions the parameters α and β were held at 1.*

		Bu$_4$NCl	Bu$_4$NBr	Bu$_3$NMeCl	Bu$_3$NMeBr	Bu$_3$NHCl	Bu$_3$NHBr
Gaussians							
A							
	A_{OKE}	0.17	0.21	0.16	0.14	0.21	0.21
	A_{IR}	7.26	17.52	0.66	0.73	0.77	0.97
	ω_o [cm^{-1}]	47.13	32.53	45.14	25.49	61.21	38.46
	γ [cm^{-1}]	40.81	25.70	44.82	33.15	51.00	40.12
B							
	A_{OKE}	0.017	0.17	0.026	0.054	0.030	0.14
	A_{IR}	2.44*10^{-09}	2.15*10^{-09}	7.45*10^{-09}	0.026	0.077	0.081
	ω_o [cm^{-1}]	121.82	61.64	77.72	57.00	131.50	72.22
	γ [cm^{-1}]	20.81	18.44	20.41	19.15	29.79	34.42
C							
	A_{OKE}	0.10	0.11	0.064	0.097	0.025	0.037
	A_{IR}	2.87	0.46	0.53	0.33	0.62	0.56
	ω_o [cm^{-1}]	88.99	84.47	105.78	77.62	174.78	121.18
	γ [cm^{-1}]	32.85	21.13	36.71	28.52	27.04	21.60
D							
	A_{OKE}	0.034	0.082	0.014	0.027	0.015	0.032
	A_{IR}	0.45	0.45	0.052	0.068	0.055	0.14
	ω_o [cm^{-1}]	141.61	104.50	153.50	116.78	221.16	151.41
	γ [cm^{-1}]	54.10	42.93	47.81	33.00	49.06	46.55
Brownians							

BO1							
	A_{OKE}	0	0	0	0	0	0
	A_{IR}	0.019	0.014	0.0027	0.0022	0.0010	0
	ω_o [cm^{-1}]	313.00	318.59	313.00	318.62	349.93	0
	γ [cm^{-1}]	30.00	17.04	30.00	33.13	29.95	0
BO2							
	A_{OKE}	0.0020	0.0031	0.0037	0.0021	0.0027	0.0049
	A_{IR}	0	0	0	0	0	0
	ω_o [cm^{-1}]	251.00	250.52	260.39	258.84	260.00	258.18
	γ [cm^{-1}]	8.00	14.99	25.79	20.03	12.00	19.11
BO3							
	A_{OKE}	0.0082	0.0077	0.0042	0.0039	0.0026	0.0019
	A_{IR}	0	0	0	0	0	0
	ω_o [cm^{-1}]	292.00	295.00	315.52	314.42	305.00	300.88
	γ [cm^{-1}]	35.00	30.02	18.91	21.92	30.00	32.03
BO4							
	A_{OKE}	0.00014	0.0067	0	0.0066	0.00044	0.00084
	A_{IR}	0	0	0	0	0	0
	ω_o [cm^{-1}]	395.00	186.57	0	167.73	395.00	399.00
	γ [cm^{-1}]	5.00	30.07	0	47.31	10.00	10.00
Debye							
	A_{OKE}	0.11	0.21	0.13	0.12	0.19	0.20
	A_{IR}	$1.23*10^{-08}$	0.10	$6.28*10^{-08}$	2.29	$6.05*10^{-07}$	$3.64*10^{-09}$
	τ [ps]	8.99	10.52	7.96	13.14	7.85	13.13
	Γ [cm^{-1}]	55.00	30.00	50.00	25.00	65.00	40.00

CALCULATION OF DIPOLE MOMENTS AND MOLECULAR POLARIZABILITIES

The permanent dipole moment vector and molecular polarizability tensor was calculated for the three cations used in this study. To speed up the calculation, it was performed for tetraethylammonium (N_{2222}), triethylmethylammonium (N_{2221}), and triethylammonium (N_{2220}) using the Gaussian 09 software package[12] with a B3LYP/6-311++G(2df,p) Polar SCRF=(PCM,Solvent=Ethanol) level of theory. The dipole moment of the cations is expressed relative to the center of nuclear charge taken as the origin of coordinates.

Tetraethylammonium (N_{2222})

There are a number of isomers all with relatively small permanent dipole moments of ~0.7 D. The eigenvalues of the polarizability tensor are 19.5, 19.1, and 18.2 Å^3. Thus, the anisotropic part of the polarizability tensor of the cation is very small (1.3 Å^3), indicating that there must be a large contribution to the polarizability from ion pairs.

Triethylmethylammonium (N_{2221})

As in the case of tetraethylammonium, the permanent dipole moment is relatively small at 1.0 D. The eigenvalues of the polarizability tensor are 17.4, 16.6, and 15.7 Å^3 resulting in a small anisotropic polarizability of only 2.1 Å^3 as in the case of tetraethylammonium.

Triethylammonium (N_{2220})

In the case of triethylammonium, the permanent dipole moment is significantly larger and depends on the isomer ranging from 2.4 to 3.4 D. The eigenvalues of the polarizability tensor are ~15, ~14.5, ~13.5 Å^3 again resulting in a small anisotropic polarizability of only 0.5 to 2.1 Å^3 (depending on isomer) as before.

MELTING POINTS

Table SI2. *Melting points of ionic liquids used in the experiments and temperatures the measurements were taken at.*

	Bu$_4$NCl	Bu$_4$NBr	Bu$_3$NMeCl	Bu$_3$NMeBr	Bu$_3$NHCl	Bu$_3$NHBr

experimental melting point [°C]	80 ± 5	120 ± 5	110 ± 5	130 ± 5	-	80 ± 5
literature melting point [°C]	83-86, 90-92	102-106, 122	108-110	120.5-121.5		
measurement taken at [°C]	90	125	120	135,145 (OKE/IR)	80	85, 100 (OKE/IR)

REFERENCES

1.	Fumino, K.; Reichert, E.; Wittler, K.; Hempelmann, R.; Ludwig, R., *Angew. Chem. Int. Ed.* **2012,** *51* (25), 6236-6236.
2.	González-Jiménez, M.; Ramakrishnan, G.; Harwood, T.; Lapthorn, A.; Kelly, S.; Ellis, E.; Wynne, K., *Nat. Commun.* **2016,** 7, 11799-11799.
3.	Turton, D. A.; Senn, H. M.; Harwood, T.; Lapthorn, A. J.; Ellis, E. M.; Wynne, K., *Nat. Commun.* **2014,** 5, 3999-3999.
4.	Giraud, G.; Wynne, K., *J. Chem. Phys.* **2003,** *119* (22), 11753-11764.
5.	Birch, J. R.; Nicol, E. A., *Infrared Phys.* **1984,** *24* (6), 573-575.
6.	Capelo, S. B.; Mendez-Morales, T.; Carrete, J.; Lago, E. L.; Vila, J.; Cabeza, O.; Rodriguez, J. R.; Turmine, M.; Varela, L. M., *J. Phys. Chem. B* **2012,** *116* (36), 11302-11312.
7.	Govinda, V.; Vasantha, T.; Khan, I.; Venkatesu, P., *Ind. Eng. Chem. Res.* **2015,** *54* (36), 9013-9026.
8.	Xu, Y.; Chen, B.; Qian, W.; Li, H., *J. Chem. Thermodyn.* **2013,** *58*, 449-459.
9.	Turton, D. A.; Wynne, K., *J. Chem. Phys.* **2008,** *128*, 154516-154516.
10.	McMorrow, D.; Lotshaw, W. T., *Chem. Phys. Lett.* **1993,** *201* (1), 369-376.
11.	Salzer, H. E., *Math. Tables Other Aids Comput.* **1951,** 5 (34), 67--70.
12.	Gaussian 09, Revision D.01, M. J. Frisch, G. W. Trucks, H. B. Schlegel, G. E. Scuseria, M. A. Robb, J. R. Cheeseman, G. Scalmani, V. Barone, B. Mennucci, G. A. Petersson, H. Nakatsuji, M. Caricato, X. Li, H. P. Hratchian, A. F. Izmaylov, J. Bloino, G. Zheng, J. L. Sonnenberg, M. Hada, M. Ehara, K. Toyota, R. Fukuda, J. Hasegawa, M. Ishida, T. Nakajima, Y. Honda, O. Kitao, H. Nakai, T. Vreven, J. A. Montgomery, Jr., J. E. Peralta, F. Ogliaro, M. Bearpark, J. J. Heyd, E. Brothers, K. N. Kudin, V. N. Staroverov, T. Keith, R. Kobayashi, J. Normand, K. Raghavachari, A. Rendell, J. C. Burant, S. S. Iyengar, J. Tomasi, M. Cossi, N. Rega, J. M. Millam, M. Klene, J. E. Knox, J. B. Cross, V. Bakken, C. Adamo, J. Jaramillo, R. Gomperts, R. E. Stratmann, O. Yazyev, A. J. Austin, R. Cammi, C. Pomelli, J. W. Ochterski, R. L. Martin, K. Morokuma, V. G. Zakrzewski, G. A. Voth, P. Salvador, J. J. Dannenberg, S. Dapprich, A. D. Daniels, O. Farkas, J. B. Foresman, J. V. Ortiz, J. Cioslowski, and D. J. Fox, Gaussian, Inc., Wallingford CT, 2013.